# The intensity and motion of hybrid cyclones in the Australian region in a composite potential vorticity framework

J. F. Quinting[a, b*], M. J. Reeder[a,c] and J. L. Catto[a, d]

[a]*School of Earth, Atmosphere and Environment, Monash University, Clayton, Victoria, Australia*

[b]*Institute of Meteorology and Climate Research (IMK-TRO), Karlsruhe Institute of Technology (KIT), Karlsruhe, Germany*

[c]*ARC Centre of Excellence for Climate Extremes, Monash University, Clayton, Victoria, Australia*

[d]*College of Engineering, Mathematics and Physical Sciences, University of Exeter, Exeter, United Kingdom*

*Correspondence to: Institute of Meteorology and Climate Research (IMK-TRO), Karlsruhe Institute of Technology (KIT), POB 3640, 76021 Karlsruhe, Germany; Email: julian.quinting@kit.edu

**Hybrid cyclones (HCs) in the Australian region typically reach their peak intensity in an amplified flow comprising upper-tropospheric ridges upstream and downstream of the cyclone and a north–south elongated trough. Nonetheless, there is considerable case-to-case variability. Taking a composite viewpoint, the present study investigates how such variations in the upper-tropospheric potential vorticity (PV) anomalies affect the subsequent intensity and motion of HCs in the Australian region. First, cyclones are grouped into four clusters with structurally-similar environments by applying a k-means clustering to the 315-K PV anomaly. The clusters reveal that HCs can be associated with a north–south elongated trough (Cluster 1), a PV cut-off (Cluster 2), and cyclonically breaking troughs (Clusters 3 and 4). Second, the effect of these features on the intensity and tracks is quantified using piecewise PV inversion. The maximum intensity of cyclones in Cluster 1 is largely determined by their upper-tropospheric cyclonic PV anomaly. Conversely, diabatically generated lower-tropospheric PV anomalies dominate the intensity of cyclones in Clusters 3 and 4. In these two clusters, the cyclonically breaking trough and a downstream ridge induce an anomalous northeasterly low-level flow across the cyclone centre. The downstream ridge is most pronounced in Cluster 4, leading to the furthest poleward cyclone displacement compared to the other clusters. In Clusters 1 and 2, the upper-level PV anomaly primarily slows the eastward motion of the cyclones. In agreement with recent idealised studies, the analysis suggests that the effect of upper-tropospheric PV anomalies on the poleward motion of HCs is analogous to the beta-gyres that influence the motion of tropical cyclones.**

 

## 1. Introduction

Cyclones possessing a lower-tropospheric warm inner core and an upper-tropospheric cold core are commonly referred to as hybrid cyclones (HCs; Spiegler 1972). The term HC includes a range of cyclone types, including extratropical transitioning tropical cyclones (e.g., Jones *et al.* 2003; Evans *et al.* 2017), subtropical cyclones (e.g., Simpson 1952; Evans and Guishard 2009), and warm-seclusion cyclones (e.g., Shapiro and Keyser 1990).

In the Australian region, heavy rainfall and storm-force winds have been linked to HCs in a number of case studies (e.g., Mills and Wu 1995; Griffiths *et al.* 1998; Mills 2001; Mills *et al.* 2010). From a climatological perspective, a companion study by Quinting *et al.* (2018) reveals that up to 90% of HCs are associated with extreme precipitation which is comparable to other non-hybrid cyclones. The study also shows that HCs frequently reach their maximum intensity over the Great Australian Bight and the Tasman Sea. Hence, they may cause floods, damaging winds and storm surges in the coastal regions of south and southeastern Australia.

HCs in the Australian region typically reach their maximum intensity in an amplified flow comprising upper-tropospheric ridges upstream and downstream of the cyclone and a north–south elongated trough associated with the cyclone itself. However, Quinting *et al.* (2018) noted considerable case-to-case variability of the upper-tropospheric potential vorticity (PV) structure, which is related to the amplitude of the ridges upstream and downstream of the cyclones as revealed by the three leading empirical orthogonal functions (EOFs) of the 315-K PV anomaly (Fig. 10 in Quinting *et al.* 2018). This case-to-case variability motivates the present study, which explicitly addresses

- the identification of typical upper-tropospheric PV structures characterising the observed case-to-case variability by applying a cluster analysis,
- the contribution of circulation anomalies to the overall cyclone intensity in a quantitative composite PV framework,
- the dependence of the cyclone motion on the identified upper-tropospheric PV structures and the sensitivity of the results to the choice of the clustering variable,
- and the mechanisms explaining the dependence of the cyclone motion on the upper-tropospheric PV structures.

One useful framework in which to analyse the dynamics of midlatitude cyclones is *PV thinking* (Hoskins *et al.* 1985). In this framework, midlatitude cyclone development can be thought of as the interaction between cyclonic PV anomalies at different levels which, in the mature phase of the cyclone, form a vertically stacked and troposphere-spanning PV tower (e.g., Hoskins 1990; Rossa *et al.* 2000; Čampa and Wernli 2012). Typically, the formation of the PV tower involves three distinct cyclonic anomalies: a positive potential temperature anomaly at the surface produced by the meridional displacement of the isentropes and corresponding to a cyclonic anomaly (Davis and Emanuel 1991), a lower-tropospheric PV anomaly, and an upper-level PV anomaly of stratospheric origin associated with the displacement of the tropopause. Although the formation of the upper-level anomaly is largely due to dry dynamics (e.g., Reed *et al.* 1992; Rossa *et al.* 2000), the lower-tropospheric cyclonic PV anomaly is predominantly generated diabatically through latent heating (e.g., Kuo *et al.* 1991; Reed *et al.* 1992; Stoelinga 1996; Wernli and Davies 1997; Ahmadi-Givi *et al.* 2004). This latent heating is particularly intense in the warm conveyor belt (WCB, e.g., Harrold 1973; Carlson 1980) so that low-level PV produced diabatically in this region can contribute to the intensification of the cyclone (Binder *et al.* 2016). The contribution of the three cyclonic PV anomalies forming the PV tower to the maximum cyclone intensity varies substantially from case to case. For example, the low-level circulation of a continental cyclone is dominated by the cyclonic anomaly associated with the positive low-level potential temperature anomaly (Davis 1992), whereas in contrast, the low-level circulation of mature marine cyclones is typically dominated by diabatically generated low-level PV anomalies (e.g., Balasubramanian and Yau 1994; Davis *et al.* 1996; Stoelinga 1996; Ahmadi-Givi *et al.* 2004; Martin and Otkin 2004).

Not only does the diabatic heating affect the cyclone intensity, it amplifies the downstream flow. For example, the diabatic heating associated with the WCB, leads to a net rearrangement of the PV characterised by a cyclonic anomaly below the heated region and an anticyclonic anomaly above it (e.g., Pomroy and Thorpe

2000; Massacand *et al.* 2001; Grams *et al.* 2011). This upper-level diabatically enhanced downstream anticyclonic anomaly, as well as the upper-level cyclonic anomaly associated with the cyclone itself, affect the motion of the cyclone. Idealised experiments and case studies show that the two anomalies form a dipole pattern centred over the low-level cyclone, and are responsible for the poleward motion of the cyclone through advection (e.g., Riviére *et al.* 2012; Oruba *et al.* 2013; Coronel *et al.* 2015; Tamarin and Kaspi 2016). The orientation of the axis of the dipole changes during the evolution of the cyclone. As the cyclone reaches its maximum intensity, the axis becomes meridionally oriented, leading to a faster poleward motion than at later stages when the axis is tilted more towards the zonal direction (Coronel *et al.* 2015; Tamarin and Kaspi 2016). As the dipole is tilted against the direction of the background flow, it also decelerates the eastward displacement of the cyclone (Coronel *et al.* 2015). In addition to the advection, diabatic processes contribute to the cyclone motion as they propagate the associated cyclonic PV anomaly eastward and poleward by strengthening the low-level cyclonic PV (Coronel *et al.* 2015; Tamarin and Kaspi 2016; Tamarin-Brodsky and Kaspi 2017). Although recent studies highlight the importance of upper-level PV anomalies in steering midlatitude cyclones poleward (e.g., Riviére *et al.* 2012; Tamarin and Kaspi 2016; Booth *et al.* 2017), the motion of midlatitude cyclones has not been systematically linked to the structure of the upper-level surrounding PV field.

This study is the first to quantify for a large number of HCs the effect of the upper-level surrounding PV field on the intensity and motion, and the approach taken is piecewise PV inversion. The cyclone tracking and HC identification, the clustering, the mathematical details of the piecewise PV inversion, and the data used in this study are described in Section 2. The dynamical processes determining the intensity and motion of HCs are presented in Section 3, including sensitivity tests concerning the choice of the cluster variables. The study ends with a concluding discussion and an outlook in Section 4.

## 2. Data and methodology

### 2.1. *Cyclone tracking and HC identification*

All analyses in this study are based on 6-hourly ERA-Interim reanalyses (Dee *et al.* 2011) regridded to a uniform 0.75° latitude–longitude grid. For a detailed description of the cyclone tracking and of the identification of the HCs, the reader is referred to the companion study by Quinting *et al.* (2018).

In brief, cyclones of all types are identified using an objective feature tracking method (Hodges 1994; 1995; 1999). The present study focuses on cyclones which are located at least once during their life cycle between 20–50°S and 100–180°E and which reach a maximum intensity of less than $-6\times10^{-5}\,\mathrm{s}^{-1}$ (greater than 6 cyclonic vorticity units; CVU) in the 850-hPa relative vorticity. From the set of all cyclones identified, the HCs are extracted using a cyclone phase space diagnostic (Hart 2003; Evans and Hart 2003) defined by three parameters. These parameters are the lower-tropospheric thermal asymmetry $B$, the lower-tropospheric thermal wind $-V_T^L$, and the upper-tropospheric thermal wind $-V_T^U$. In this study, HCs are defined as cyclones for which $B < 10$, $-V_T^L > 0$ and $-V_T^U < 0$, meaning, they are characterised by a lower-tropospheric symmetric warm-core and an upper-tropospheric cold core. For the period May–September 1979–2010, Quinting *et al.* (2018) identified 573 HCs, and these form the basis of the present study.

### 2.2. *Cyclone clustering*

Once the HCs are identified in the ERA-Interim data, cyclones in a structurally-similar environment are grouped using a k-means clustering (Hartigan and Wong 1979; Catto 2018) of the 315-K PV anomaly within 2000 km of the cyclone centre at its maximum intensity. This anomaly is defined relative to the monthly climatology. The number of clusters is chosen a-priori and the choice tested for 2–10 clusters. One measure of the correct choice is the distance of dissimilarity metric (Stefanon *et al.* 2012; Lee and Grotjahn 2016), which is defined as the minimum of the average inter-cluster distance, where the inter-cluster distance between a member $\boldsymbol{q}$ in cluster $c_q$ and a member $\boldsymbol{p}$ in cluster $c_p$ is

$$d(\boldsymbol{p}, \boldsymbol{q}) = 1 - r(\boldsymbol{p}, \boldsymbol{q}) \quad (1)$$

and

$$r(\boldsymbol{p},\,\boldsymbol{q}) = \frac{\sum_{i=1}^{N}\sum_{j=1}^{M} p_{i,j}q_{i,j}}{\left(\sum_{i=1}^{N}\sum_{j=1}^{M} p_{i,j}^2\right)^{\frac{1}{2}}\left(\sum_{i=1}^{N}\sum_{j=1}^{M} q_{i,j}^2\right)^{\frac{1}{2}}} \quad (2)$$

is the anomaly correlation coefficient. The elements $p_{i,j}$ and $q_{i,j}$ are the values of $\boldsymbol{p}$ and $\boldsymbol{q}$ at coordinates $(i,\,j)$ along the longitudinal and latitudinal axes of dimension $M$ and $N$, respectively. The minimum of the average inter-cluster distances computed pairwise between all members of two different clusters yields the dissimilarity index. The higher the dissimilarity index, the more distinct the individual clusters. The dissimilarity index is smallest for 5 clusters and stays nearly constant as the number of clusters is increased (not shown), implying that more than 4 clusters does not introduce new patterns, but instead splits similar patterns. In the present study, 4 clusters are used since fewer clusters miss one of the synoptically distinct features described in Section 3.1 while more produced essentially repeated patterns.

### 2.3. *Piecewise potential vorticity inversion*

Piecewise potential vorticity inversion (PPVI) is a valuable tool for isolating the effects of individual PV anomalies on the dynamics of midlatitude cyclones. Given a balance condition and suitable boundary conditions, the kinematic and thermodynamic structure of the flow can be determined from the PV distribution alone. The formulation and method for the PPVI used here are due to Davis and Emanuel (1991) and are very briefly outlined now.

Assuming hydrostatic balance and that the magnitude of the irrotational component of the wind is much smaller than the non-divergent component, the PV can be expressed approximately as

$$PV = \frac{g\kappa\pi}{p}\left[(f+\nabla^2\Psi)\frac{\partial^2\Phi}{\partial\pi^2} - \frac{1}{a^2\cos^2\phi}\frac{\partial^2\Psi}{\partial\lambda\partial\pi}\frac{\partial^2\Phi}{\partial\lambda\partial\pi} - \frac{1}{a^2}\frac{\partial^2\Psi}{\partial\phi\partial\pi}\frac{\partial^2\Phi}{\partial\phi\partial\pi}\right], \quad (3)$$

where $\Phi$ is the geopotential, $\Psi$ is the streamfunction for the non-divergent part of the wind, $f$ is the Coriolis parameter, $\kappa = R/c_p$, $R$ is the dry gas constant, $c_p$ is the specific heat at constant pressure $p$, $\pi = c_p(p/p_0)^{\kappa}$ is the Exner function, and $p_0 = 1000$ hPa. Likewise, the balance condition, due to Charney (1955), can be written

$$\nabla^2\Phi = \nabla\cdot(f\nabla\Psi) + \frac{2}{a^4\cos^2\phi}\frac{\partial(\partial\Psi/\partial\lambda,\;\partial\Psi/\partial\phi)}{\partial(\lambda,\;\phi)}. \quad (4)$$

$\Psi$ and $\Phi$ are prescribed on the lateral boundaries and their vertical derivatives, $\partial\Phi/\partial\pi = -\theta$ and $\partial\Psi/\partial\pi = -\theta/f$, are specified at the top and bottom boundaries. Equations 3 and 4 are then solved by successive over-relaxation. To ensure convergence, the fields of PV and potential temperature are regularised, meaning that positive values of the PV (in the Southern Hemisphere) are set to –0.01 PVU and statically unstable layers are made very slightly stable.

To isolate the PV anomalies, the PV is first decomposed into a basic state and a perturbation there from (Davis and Emanuel 1991; Martin and Otkin 2004; Teubler and Riemer 2015), with the perturbation defined as the deviation of the instantaneous PV from its 14-day running mean. These time means are computed for each cyclone.

Following earlier studies (e.g., Davis and Emanuel 1991; Martin and Marsili 2002; Martin and Otkin 2004), the perturbation PV field is partitioned into an upper layer $U_{pert}$, an interior layer $M_{pert}$, and a surface layer $S_{pert}$. The surface layer comprises the 925-hPa perturbation potential temperature, which provides the lower boundary condition, and the perturbation PV at 900 hPa, which is the first level above the lower boundary. The interior layer includes all perturbation PV between 850–550 hPa. A composite vertical cross-section of all HCs reveals that anomalies of cyclonic PV that are connected to the stratospheric PV reservoir do not extend below 500 hPa (see Fig. 8 in Quinting *et al.* 2018). Hence, cyclonic PV perturbations in the interior layer are likely to be attributable to non-PV-conserving processes such as diabatic heating. The upper layer includes the remaining perturbation PV between 500–150 hPa.

The winds associated with each perturbation are derived from the corresponding perturbation stream function $\Psi'$ through the expressions

$$u' = -\frac{1}{a}\frac{\partial\Psi'}{\partial\phi}, \quad v' = \frac{1}{a\cos\phi}\frac{\partial\Psi'}{\partial\lambda}, \quad (5)$$

where the primes denote perturbations from the 14-day time mean.

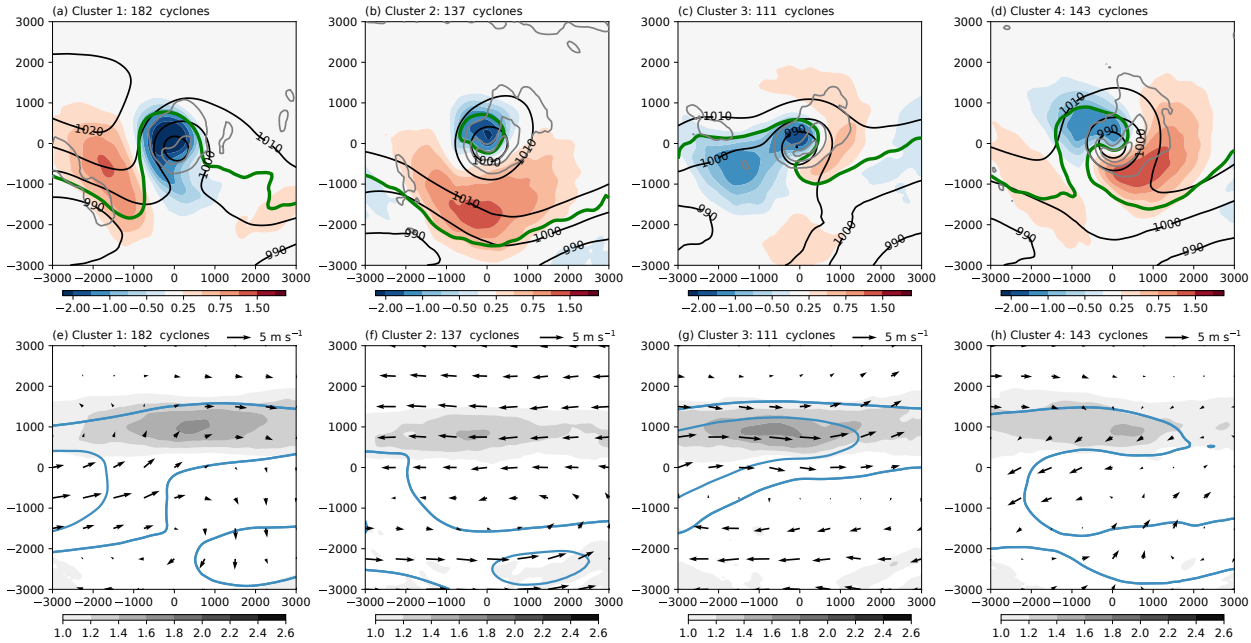


**Figure 1.** (a–d) Composite fields of HCs at maximum intensity for Clusters 1–4. Potential vorticity anomalies at 315 K relative to the monthly climatology (shading in PVU), the –2-PVU isoline at 315 K (green contour), mean sea level pressure (black contours in hPa), and mean 6-hourly precipitation (grey contours at $1, 3, 5$ mm $(6\,\mathrm{h})^{-1}$). (e–h) Composites of the time-mean basic state, defined as the 14-day running mean at 315 K (blue contours are isotachs at 20 and 25 m s$^{-1}$) for Clusters 1–4. The difference between the time-mean basic state for HCs in Clusters 1–4 and the time-mean basic state for all HCs is shown as vector winds (reference vector in panels). Shading denotes the 400–200-hPa layer-mean PV gradient of the time-mean basic state (PVU $10^{-6}\,m^{-1}$). The 315-K isentropic level corresponds to a pressure level of about 300 hPa at the cyclone centre (see Fig. 8 in Quinting *et al.* 2018). Coordinates are in km relative to the cyclone centre.

To attribute the intensity and the motion of the cyclones to individual PV anomalies the PPVI is applied to each of the 573 HCs. The PV inversion domain is zonally centred on each cyclone and extends 180° in west–east direction and from 15–81°S in north–south direction. In the vertical, the inversion domain is every 50 hPa between 950–150 hPa.

## 3. Results

### *3.1. Basic state and cyclone structure*

Decomposing all HCs into 4 clusters yields distinct upper-tropospheric patterns of PV (Fig. 1a–d) including a north–south elongated trough (Cluster 1), a PV cut-off (Cluster 2), and cyclonically breaking troughs (Clusters 3 and 4). As discussed below, these structures are consistent with the respective basic states for each cluster, defined as the 14-day running mean centred on the time of maximum intensity of each cyclone.

Cluster 1 comprises 182 cyclones (approximately 32% of all cyclones), and is characterised by a pronounced upstream ridge (red shading in Fig. 1a), a positively tilted north–south elongated trough, and a weakly amplified flow downstream. In the basic state for Cluster 1 (Fig. 1e), an anticyclonic perturbation circulation lies upstream of the cyclone, consistent with a positively tilted PV streamer. The most cyclonic upper-tropospheric PV, which is less than –2 PVU, lies on the equatorward flank of the sea level pressure minimum, which is itself less than 990 hPa (black contours in Fig. 1a). Moreover, the maximum in precipitation occurs on the poleward flank of the cyclone. In a radius of 500 km around the cyclone centre, the average precipitation is 2.9 mm $(6\,\mathrm{h})^{-1}$ with the 10th and 90th percentiles reaching from 1.8 to 4.2 mm $(6\,\mathrm{h})^{-1}$ (not shown). This cluster produces the least precipitation of the four, which is consistent with the observation that Cluster 1 cyclones reach their maximum intensity in a relatively cold and dry environment compared to climatology and to the remaining clusters (Figs. 2a, b).

Moreover, the surface- and interior-layer PV anomalies relative to the monthly climatology in a radius of 200 km around the cyclone centre are the weakest of all clusters (Fig. 2c). To the extent that the vertical PV structure in a radius of 200 km around the cyclone centre can be identified as the diabatically-generated PV tower (Čampa and Wernli 2012), the weaker surface- and interior-layer PV anomalies in Cluster 1 is consistent with lower precipitation compared to Clusters 2–4.

The composite for the 137 cyclones in Cluster 2 is characterised by an upper-level PV cut-off that is flanked by an anticyclonic PV anomaly of more than 1 PVU on its poleward side (Fig. 1b). The proximity of the PV cut-off to the mean sea level pressure

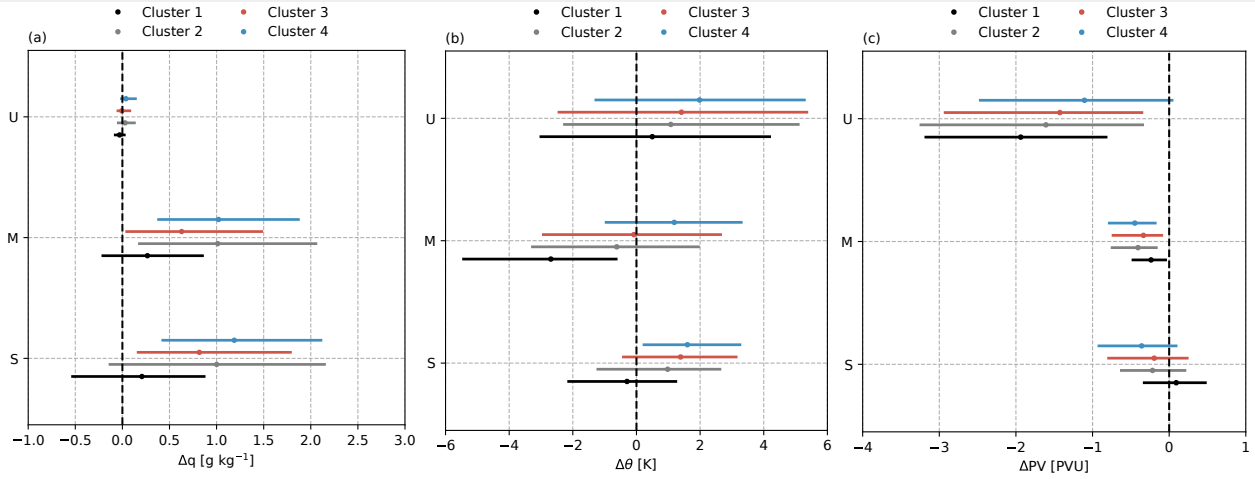


**Figure 2.** (a) Specific humidity anomaly $\Delta$q (g kg$^{-1}$), (b) potential temperature anomaly $\Delta\theta$ (K) relative to the monthly climatology in a radius of 500 km around the cyclone centre, and (c) PV anomaly $\Delta$PV (PVU) relative to the monthly climatology in a radius of 200 km around the cyclone centre at maximum intensity for the surface layer (S), interior layer (M), and upper layer (U). The dots denote the median values and the whiskers include the 10th and 90th percentiles.

minimum indicates the relatively barotropic structure of the cyclones in this cluster at the time of maximum intensity. In contrast to the other clusters, an anticyclonic circulation basic state perturbation southeast of the cyclone promotes anticyclonic wave breaking, leading to PV streamers that eventually cut off (Fig. 1g).

Cluster 3 comprises 111 cyclones (approximately 19% of all cyclones). In contrast to Clusters 1 and 2, there is a cyclonic PV anomaly upstream of the composite cyclone in Cluster 3. At lower and upper levels, the upstream flow is zonally oriented (Fig. 1c). A tongue of cyclonic (anticyclonic) PV to the north (south) of the cyclone centre is an indication of a cyclonically breaking trough. The basic state for Cluster 3 is characterised by large-scale cyclonic shear, which accounts for the cyclonically breaking trough (Fig. 1f). As with Clusters 1 and 2, the precipitation occurs predominantly on the poleward flank of the cyclone.

Large-scale cyclonic Rossby wave breaking characterises the upper-level flow of the remaining 143 cyclones comprising Cluster 4 (Fig. 1d; approximately 25% of all cyclones). Cluster 4 has a cyclonic basic state perturbation circulation upstream of the cyclone (Fig. 1h), which is consistent with the strong cyclonic wave breaking. The process of cyclonic wave breaking leads to the development of a pronounced downstream ridge at upper levels and at the surface. The precipitation in Cluster 4 falls along the bent-back warm front to the south of the cyclone centre and is the largest of any cluster. In a radius of 500 km around the cyclone centre, the average precipitation is 3.7 mm (6 h)$^{-1}$ with the 10th and 90th percentiles ranging from 1.6 to 6.2 mm (6 h)$^{-1}$ (not shown). The enhanced precipitation compared to the other clusters is likely related to a warmer and moister surface layer and interior layer in which the cyclones reach their peak intensity (Figs. 2a, b). For example, the mean surface-layer specific humidity anomaly reaches more than 1 g kg$^{-1}$, exceeding that in Cluster 1 by a factor of 3. Consistently, cyclones in Cluster 4 exhibit the most cyclonic surface- to interior-layer PV of all clusters (Fig. 2c), pointing to the relative greater importance of diabatic processes.

### 3.2. *Cyclone intensity*

Using PPVI, we assess now the contribution from individual PV anomalies to the intensity of the HCs at the time of their maximum intensity. Here intensity is measured by the 900–700-hPa layer relative vorticity perturbation at the cyclone centre. Equations 3 and 4 are nonlinear and consequently the relative vorticity induced by U$_{pert}$, M$_{pert}$ and S$_{pert}$ need not sum to the original vorticity field. However, the sum of the relative vorticity induced by U$_{pert}$, M$_{pert}$ and S$_{pert}$ explains at least 87% of the total 900–700-hPa vorticity perturbation at the cyclone centre in each cluster (i.e. the sum of percentages in Fig. 3 are at least 87% for each cluster). That most of the 900–700-hPa vorticity perturbation can be recovered implies that the total circulation can sensibly be thought of as a superposition of that attributed to the individual PV anomalies U$_{pert}$, M$_{pert}$ and S$_{pert}$.

The intensity of cyclones in Cluster 1 is dominated by the upper-level PV perturbation. On average 51% ($\sim$ 5.5 CVU) of the 900–700-hPa vorticity perturbation can be attributed to U$_{pert}$ associated with the upper-level trough (Fig. 3a). The circulation

 

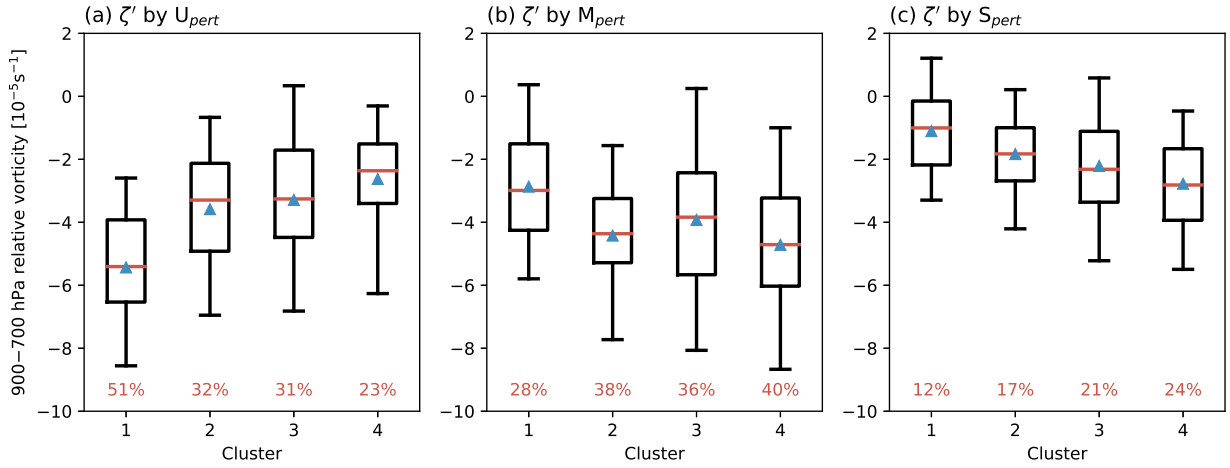


**Figure 3.** Distribution of the 900–700-hPa relative vorticity perturbations ($10^{-5}$ s$^{-1}$) associated with (a) U$_{pert}$, (b) M$_{pert}$, and (c) S$_{pert}$ at the cyclone centre at maximum intensity for Clusters 1–4. Blue triangles denote the mean, red bars the median, boxes the interquartile range, and whiskers the 5th and 95th percentiles of the distribution. Percentages give the mean contribution of U$_{pert}$, M$_{pert}$, S$_{pert}$ to the 900–700-hPa relative vorticity at the cyclone centre.

anomalies associated with the trough and the upstream upper-level ridge induce a southerly flow west of the cyclone centre (Fig. 4a). This flow creates a negative temperature anomaly at the surface (not shown), which is reflected in the anticyclonic flow anomaly induced by S$_{pert}$ immediately west of the cyclone centre (Fig. 4i). Since this anticyclonic anomaly is most pronounced in Cluster 1 (cf. panels of bottom row in Fig. 4), it is likely the result of a negative temperature anomaly due to cold air advection in a southerly flow induced by the upper-level upstream ridge and by the cyclone itself. The positive temperature anomaly on the eastern flank of the cyclone, likely due to warm air advection in a northerly flow, contributes only 12% (∼1 CVU) to the vorticity anomaly (Fig. 3c). The remaining contribution of about 28% (∼3 CVU) is attributable to M$_{pert}$ (Fig. 3b), which presumably is due to diabatic processes. Although there is variability across the individual cases in Cluster 1 (Fig. 3), the average contribution of U$_{pert}$ (M$_{pert}$) to the cyclone intensity is the strongest (weakest) of all clusters and coincides with the most (least) cyclonic upper-layer (surface- to interior-layer) PV anomaly compared to the remaining clusters (Fig. 2c). This result suggests that the contribution of diabatic processes to the cyclone intensity is relatively weak, which is in line with the lowest precipitation of all clusters (Fig. 1a–d).

Cluster 2 cyclones have the second most cyclonic upper-tropospheric PV anomaly (Fig. 2c), and the average contribution of this upper-level PV anomaly to the 900–700-hPa vorticity is the second strongest of all clusters (Fig. 3a). U$_{pert}$ induces a low-level cyclonic flow that is displaced to the north of the cyclone centre (Fig. 4b). The anomaly contributes 32% (∼3 CVU) to the 900–700-hPa vorticity field. A broad upper-level ridge poleward of the Cluster 2 cyclones induces a low-level anticyclonic flow anomaly (Fig. 4b). As will be shown in Section 3.6, this broad anticyclonic anomaly strongly affects the motion of the cyclones in Cluster 2. With 38% (∼4.5 CVU), the contribution of the mid-level PV anomaly to the 900–700-hPa vorticity field is larger than in Cluster 1, which is consistent with the vertical PV anomaly profiles in Fig. 2c. This strengthening may be due to enhanced diabatic processes as indicated by greater precipitation to the south of cyclones in Cluster 2 (Fig. 1b). The low-level potential temperature and PV perturbations S$_{pert}$ contribute 17% (∼1.5 CVU) to the 900–700-hPa vorticity (Fig. 3c), which is a larger contribution than in Cluster 1. Whether this is due to enhanced advection of warm air masses in a northerly flow or due to enhanced surface fluxes is beyond the scope of this study.

U$_{pert}$ contributes only about 31% (∼3 CVU) to the 900–700-hPa vorticity of Cluster 3 cyclones (Fig. 3a). The induced cyclonic vorticity anomaly at the cyclone centre is part of a broader cyclonic anomaly (Fig. 4c) related to the upstream trough. The vorticity perturbation induced by M$_{pert}$ is larger than in Cluster 1 (Fig. 4g) and it contributes 36% (∼3 CVU) to the 900–700-hPa vorticity anomaly (Fig. 3b). In total, M$_{pert}$ and S$_{pert}$ (Figs. 3b, c) contribute 57% to the 900–700-hPa vorticity anomaly. Hence, the

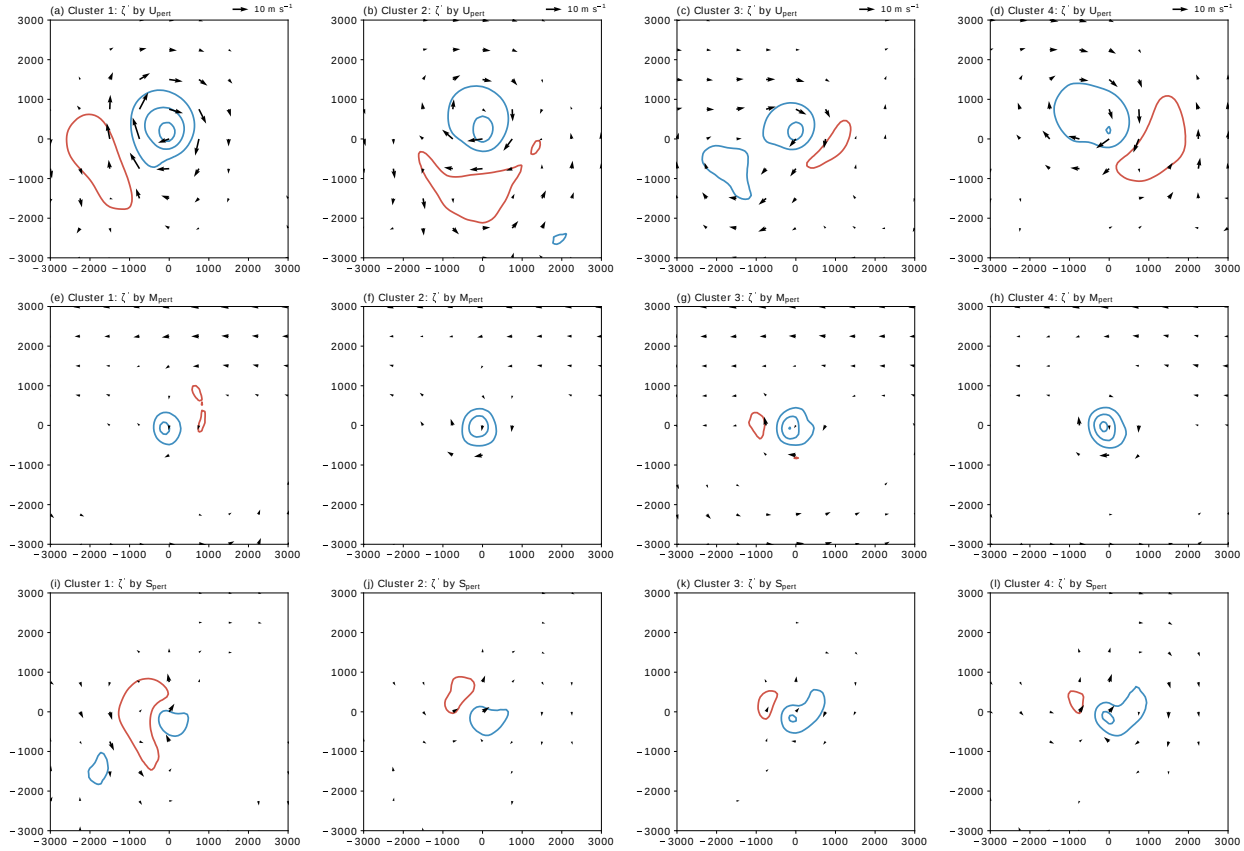


**Figure 4.** Composite fields of the 900–700-hPa relative vorticity perturbations (contoured every $2\times10^{-5}$ s$^{-1}$ with cyclonic anomalies in blue) and 900–700-hPa wind perturbations (reference vector in panels a–d) associated with (top row) $U_{pert}$, (middle row) $M_{pert}$, and (bottom row) $S_{pert}$ at maximum intensity for Clusters 1–4 as given in subcaptions. Wind vectors are only shown where wind speed greater than 2 m s$^{-1}$. Coordinates are in km relative to the cyclone centre.

circulation of Cluster 3 cyclones is more strongly determined by the lower to middle troposphere than that of Cluster 1 cyclones.

Like Cluster 3, the 900–700-hPa vorticity field of cyclones in Cluster 4 is dominated by $M_{pert}$ (Fig. 4h) and $S_{pert}$ (Fig. 4l). In total, these anomalies contribute 64% to the 900–700-hPa vorticity field (Figs. 3b, c) with the strongest contribution of 40% coming from the mid-level anomaly. This is the largest contribution from $M_{pert}$ compared to any cluster, and is consistent with the most cyclonic mid-level PV anomaly in the vertical profiles (Fig. 2c). Likewise, the $S_{pert}$ contribution of 24% (∼3 CVU) is the largest of all clusters and is consistent with the warmest near-surface temperature anomaly (Fig. 2b). The cyclonically breaking upstream trough induces a low-level cyclonic field northwest of the cyclone (Fig. 4d). The ridge that forms downstream of the cyclone as part of the wave breaking induces an anticyclonic flow anomaly to its southeast. The resulting northeasterly flow across the cyclone affects its motion as will be discussed in detail below in Section 3.6.

### 3.3. *Cyclone motion*

In the interval 2 days before to 2 days after the time of maximum intensity (–48 h to 48 h), the cyclones in the individual clusters show distinct tracks (Fig. 5). The average direction of motion of cyclones in Cluster 1 is relatively zonal from west to east (Fig. 5a) and slightly equatorward. From –48 h to 48 h the average longitudinal displacement of the cyclones in Cluster 1 is about 5500 km, making them together with Cluster 3 cyclones (Fig. 5c) the fastest moving cyclones. In contrast to Cluster 1 cyclones, cyclones in Cluster 3 move poleward by about 700 km (Fig. 5c). Although there is considerable variability in the motion of the individual cyclones comprising Cluster 2 (Fig. 5b), their zonal speed is much lower than of those comprising Clusters 1 and 3. Between –48 h and 48 h, Cluster 2 cyclones are displaced zonally by about 3000 km on average. The average meridional displacement is poleward by about 400 km prior to maximum intensity and mostly zonal afterwards. Cluster 4 cyclones exhibit the largest meridional displacement between –48 h and 48 h (Fig. 5d). During the 48 hours prior to maximum intensity, the cyclones are displaced meridionally by 1000 km on average. This

 

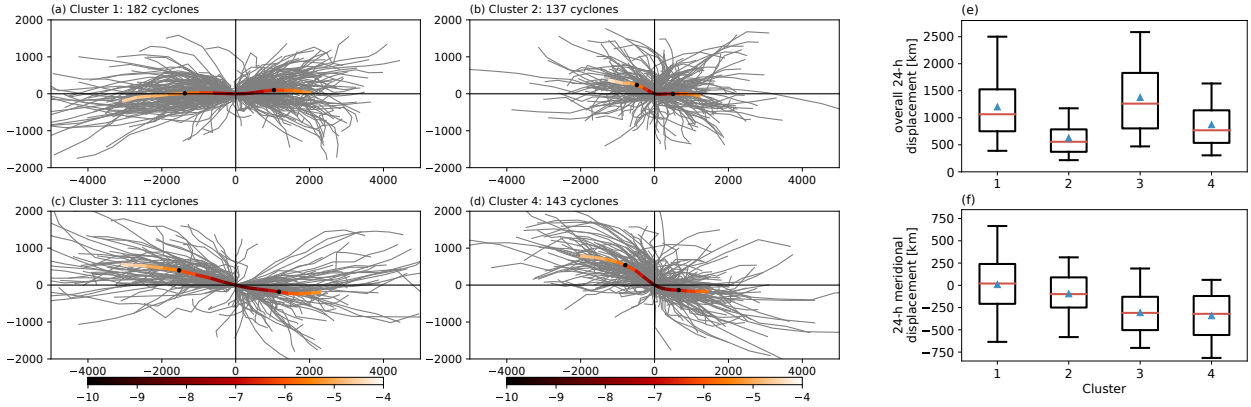


**Figure 5.** (a)–(d) Individual cyclone tracks for Clusters 1–4 (grey lines) and mean cyclone track colored by relative vorticity ($10^{-5}$ s$^{-1}$) from –48 h to 48 h relative to the cyclone position at maximum intensity. Black dots mark average cyclone positions at –24 h and 24 h, respectively. As some cyclones have a lifetime of less than 96 h, the sample size that forms the basis of the mean cyclone track varies with time. Coordinates are in km relative to the cyclone centre. (e, f) Box and whisker plots of the (e) overall cyclone displacement (in km) and (f) meridional displacement (in km) from -12 to 12 h. Blue triangles denote the mean, red bars the median, boxes the interquartile range, and whiskers the 1st and 99th percentiles of the distribution.

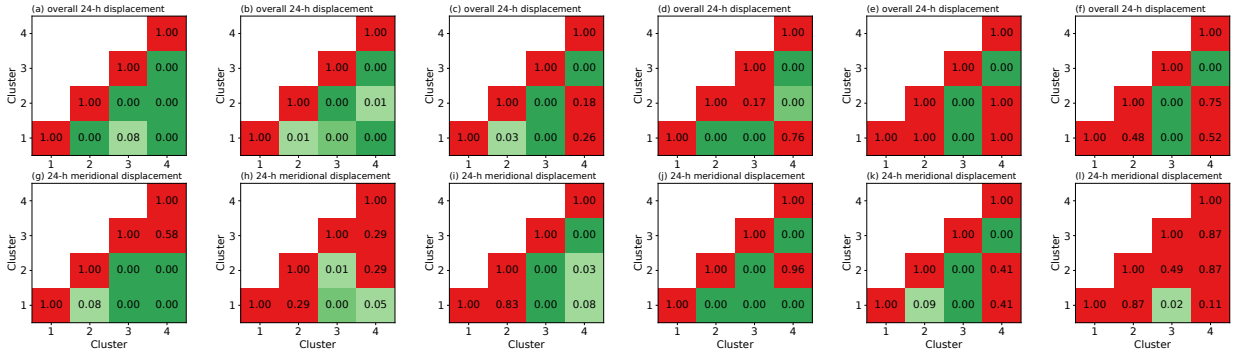


**Figure 6.** Results of a Kruskal-Wallis post-hoc pairwise Dunn's test for (top row) overall cyclone displacement and (bottom row) meridional cyclone displacement from –12 h to 12 h. The test is applied to 4 Clusters identified based on (a, g) 315-K PV anomaly relative to the monthly climatology, (b, h) 500–150 hPa layer-mean PV anomaly relative to the monthly climatology, (c, i) 500–150 hPa layer-mean PV, (d, j) 600–300 hPa layer-mean PV, (e, k) pressure on the dynamic tropopause, and (f, l) potential temperature on the dynamic tropopause. The colors refer to different significance levels (red: p-value $>$ 0.1, light green: 0.01 $<$ p-value $\leq$ 0.1, green: 0.001 $<$ p-value $\leq$ 0.01, dark green: p-value $<$ 0.001).

meridional motion continues after maximum intensity, although it is generally slower. Cluster 4 cyclones move relatively slowly in the zonal direction, covering 3500 km on average in four days.

The remaining analysis of the cyclone motion focuses on the day centred on the maximum intensity (from –12 h to 12 h). As for the four-day period around maximum intensity, HCs in Clusters 1 and 3 exhibit the largest overall displacement (Fig. 5e). The average 24-h displacement is 1200 and 1400 km, respectively, with the interquartile range extending from around 800 km to 1800 km. In contrast, the overall 24-h displacement of cyclones in Clusters 2 and 4 is on average 500 and 750 km, respectively. For cyclones in Cluster 2, the interquartile range extends only from 400 to 800 km.

To test the null-hypothesis that the median of the overall 24-h displacement of the 4 clusters is identical, we apply a Kruskal-Wallis test (Kruskal and Wallis 1952). As the p-value is less than 0.01 (not shown), we reject the null-hypothesis and conclude that the 24-h displacement of at least two clusters is significantly different. A final post-hoc pairwise Dunn's test reveals which of the Clusters 1–4 are significantly different. Concerning the overall 24-h displacement, all clusters except for Clusters 1 and 3 are statistically significantly different at the 99.9 percentile confidence level (Fig. 6a). As for the full period from –48 h to 48 h, the direction of motion of cyclones in Cluster 1 is relatively zonal from -12 to 12 h. The mean meridional displacement is close to zero (Fig. 5f). The cyclones in the remaining clusters are displaced poleward by 100 km (Cluster 2) to 300 km (Cluster 4). This meridional displacement is statistically significant between all clusters except for Clusters 1/2 and Clusters 3/4 (Fig. 6g).

Simulations with a quasigeostrophic baroclinic two-layer model (Gilet *et al.* 2009) and numerical sensitivity experiments for a selected European winter storm (Riviére *et al.* 2012) suggested that the poleward displacement of a cyclone is related to the vertically-averaged upper-tropospheric PV gradient of the

time-averaged background flow. They found that the greater the gradient, the faster the poleward displacement of the cyclones due to an enhanced downstream ridge advecting the surface cyclone poleward. However, for HCs in the Australian region, the dependence of the poleward displacement on the 400–200-hPa layer-mean PV gradient (shading in Fig. 1e–h) is equivocal. For example, the time-mean basic state PV gradient for Cluster 4, the cluster with the fastest poleward moving cyclones, is similar to that for Cluster 1 (Fig. 1e) and Cluster 2 (Fig. 1f). On the other hand, the time-mean basic state PV gradient for the Cluster 3, the cluster with the second fastest poleward moving cyclones, is associated with the strongest PV gradient (Fig. 1g).

### 3.4. *Sensitivity to the choice of variables clustered*

It is remarkable that clustering the 315-K PV anomalies results in statistically significantly different cyclone tracks around the time of maximum intensity. To test whether this result is specific to the 315-K PV anomalies or whether similar results can be found for different cluster variables, we apply the k-means clustering to: the 500–150 hPa layer-mean PV anomaly relative to the monthly climatology, the 600–300 hPa layer-mean PV, the 500–150 hPa layer-mean PV, pressure on the dynamic tropopause, and potential temperature on the dynamic tropopause in a radius of 2000 km around the cyclone centre. As before, the cluster number is set to 4 and the overall cyclone displacement and the meridional cyclone displacement are investigated from –12 h to 12 h. A post-hoc pairwise Dunn's test is applied to test the null-hypothesis that the median of the overall 24-h displacement of the four clusters is identical. The analysis reveals that none of these cluster variables separates the tracks around the time of maximum intensity as well as the 315-K PV anomaly. For instance, the 500–150 hPa layer-mean PV anomaly separates tracks reasonably well in terms of their overall 24-h displacement (Fig. 6b), but only in three out of six cluster combinations the meridional displacement differs significantly (Fig. 6h). Similar results are found for the 500–150 hPa layer-mean PV (Figs. 6c, i), the 600–300 hPa layer-mean PV (Figs. 6d, j), and pressure on the dynamic tropopause (Figs. 6e, k). Like the 315-K PV anomalies, the 600–300 hPa layer-mean PV separates reasonably well the meridional cyclone displacement

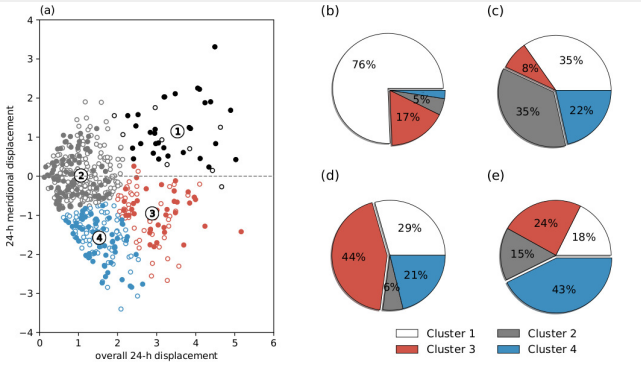


**Figure 7.** Results of k-means clustering applied to the overall cyclone displacement and the meridional cyclone displacement from –12 h to 12 h divided by their respective standard deviation. Filled circles indicate cyclones that fall into the same cluster when clustering the 315-K PV anomaly. Circled numbers show the cluster centroids of Track-Clusters 1–4. Pie charts of the fraction of the clusters based on the 315-K PV anomaly falling into (b) Track-Cluster 1, (c) Track-Cluster 2, (d) Track-Cluster 3, and (e) Track-Cluster 4.

(Fig. 6j). Presumably, this result is related to the height of the 315-K isentrope which falls into this layer (Fig. 8b in Quinting *et al.* 2018). The worst separation in terms of cyclone displacement comes from clustering the potential temperature on the dynamic tropopause (Figs. 6f, l).

### 3.5. *Sensitivity to clustering on the cyclone tracks*

Clustering the 315-K PV anomaly yields four clusters with characteristic patterns of PV anomaly and significantly different tracks between –12 h and 12 h. In the following we ask whether the reverse is true: whether clustering the tracks directly yields similar PV anomaly patterns and similar groups of tracks. The reversibility of the clustering is to some degree a test of the robustness of the clusters found and hence a test of the robustness of the physical attributes attached to them. To this end, a k-means clustering with four clusters is applied to the overall cyclone displacement and the meridional displacement from –12 h to 12 h. These clusters are referred to as Track-Clusters 1–4. Track-Cluster 1 comprises 41 cyclones that move fast in the zonal direction and slightly equatorward (black circles Fig. 7a). As for Cluster 1, the upper-tropospheric flow is characterised by a pronounced upstream ridge that is presumably diabatically amplified as indicated by an average precipitation of more than 1 mm $(6\,\mathrm{h})^{-1}$ on its western flank (Fig. 8a). The cyclone is associated with a cyclonic 315-K PV anomaly of less than –2 PVU located equatorward of the mean sea level pressure minimum. The precipitation associated with the cyclone is smallest compared to

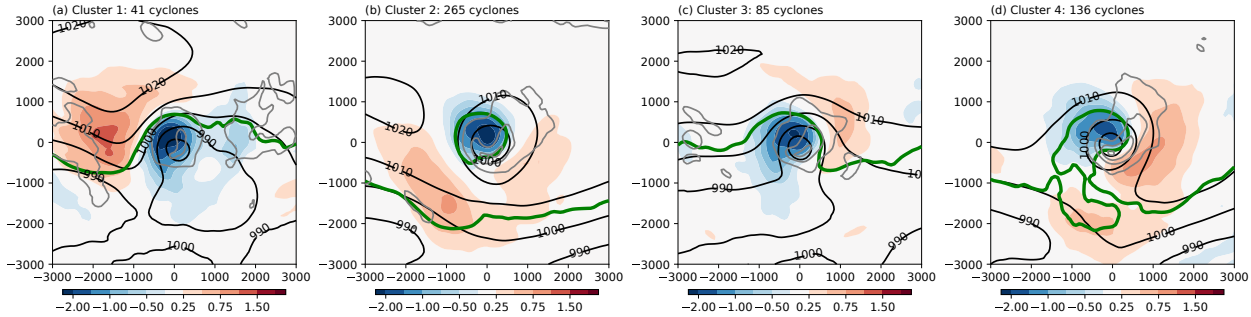


**Figure 8.** As in Fig. 1a–d, but for Track-Clusters 1–4.

the remaining Track-Clusters. There are 85 cyclones in Track-Cluster 3 and they move poleward and rapidly eastward. The 315-K PV anomalies, which mark a cyclonically breaking trough and a downstream ridge (Fig. 8c), are strikingly similar to those in Cluster 3, supporting the interpretation that this upper-level PV structure is characteristic of cyclones that move rapidly in west–east direction and slightly poleward. Track-Clusters 2 and 4 comprise 265 and 136 cyclones, respectively. Their overall displacement is comparatively small. As for the clusters based on the 315-K PV anomaly, the slowest moving cyclones in Track-Cluster 2 are associated with an upper-tropospheric PV cut-off (Fig. 8b). Track-Cluster 4 cyclones exhibit the greatest poleward displacement, and thus are most similar to cyclones in Cluster 4. Their 315-K PV structure is also similar to Cluster 4, and shows a cyclonically breaking trough and a pronounced downstream ridge (Fig. 8d). Likewise, cyclones in Track-Cluster 4 are associated with the largest precipitation of all Track-Clusters.

Qualitatively, the cyclone tracks and the 315-K PV anomalies in the four Track-Clusters are similar to Clusters 1–4 based on the 315-K PV anomaly. This impression is confirmed when quantifying the fraction of cyclones in Clusters 1–4 being part of Track-Clusters 1–4. Of the cyclones in Track-Cluster 1, 76% are also in Cluster 1 (Fig. 7b), in agreement with the observation that cyclones in these two clusters propagate rapidly in a mostly zonal direction. The cyclones in Track-Cluster 2 are mostly spread across Clusters 1, 2, and 4 (Fig. 7c). Thus, their relation to a characteristic upper-level PV structure is less clear than for the other Track-Clusters. Cyclones in Cluster 3 are characterised by a rapid west–east and slightly poleward displacement. The resemblance of this cluster to Track-Cluster 3 is corroborated by the fact that cyclones in Cluster 3 account for 44% of the cyclones in Track-Cluster 3 (Fig. 7d). Finally, Cluster 4 accounts for 43% of the cyclones in Track-Cluster 4 (Fig. 7e), indicating that cyclones exhibiting the largest poleward displacement are associated with a cyclonically breaking trough and a pronounced downstream ridge. That two very different clustering approaches yield similar results strengthens the idea that the tracks of the HCs are strongly tied to the 315-K PV structure.

### 3.6. *The relationship between the PV anomalies and the tracks*

The contribution of the PV perturbations identified in Section 3.2 to the cyclone displacement is analysed now. The analysis is based on the flux form of the vorticity tendency equation (Haynes and McIntyre 1987) in spherical coordinates

$$\begin{aligned}\frac{\partial \eta}{\partial t} = & \underbrace{-\frac{1}{a\cos\phi}\frac{\partial}{\partial\lambda}(\bar{u}\eta) - \frac{1}{a}\frac{\partial}{\partial\phi}(\bar{v}\eta)}_{A_\zeta} \\ & \underbrace{-\frac{1}{a\cos\phi}\frac{\partial}{\partial\lambda}(u'\eta) - \frac{1}{a}\frac{\partial}{\partial\phi}(v'\eta)}_{B_\zeta} \\ & \underbrace{-\frac{1}{a\cos\phi}\frac{\partial}{\partial\lambda}(\omega\frac{\partial v}{\partial p}) + \frac{1}{a}\frac{\partial}{\partial\phi}(\omega\frac{\partial u}{\partial p})}_{C_\zeta} + D\,. \end{aligned} \tag{6}$$

Here $\eta$ is the absolute vorticity, $\omega$ is the vertical motion in pressure coordinates, and $D$ is the dissipation, which is not considered in the remainder of the analysis. The first four terms on the right-hand side describe the divergence of the horizontal advective flux of absolute vorticity. Here the horizontal flow is decomposed into the time-mean basic state ($\bar{u}$, $\bar{v}$) and deviations there from ($u'$, $v'$) induced by the perturbation PV. Consequently, the first two terms on the right-hand side describe the divergence of the vorticity flux by the basic state, while the third and fourth term on the right-hand side are the divergence of the vorticity advective flux due to the PV perturbation field. To quantify the contributions of $\mathrm{U}_{pert}$ and $\mathrm{S}_{pert}$, we distinguish between

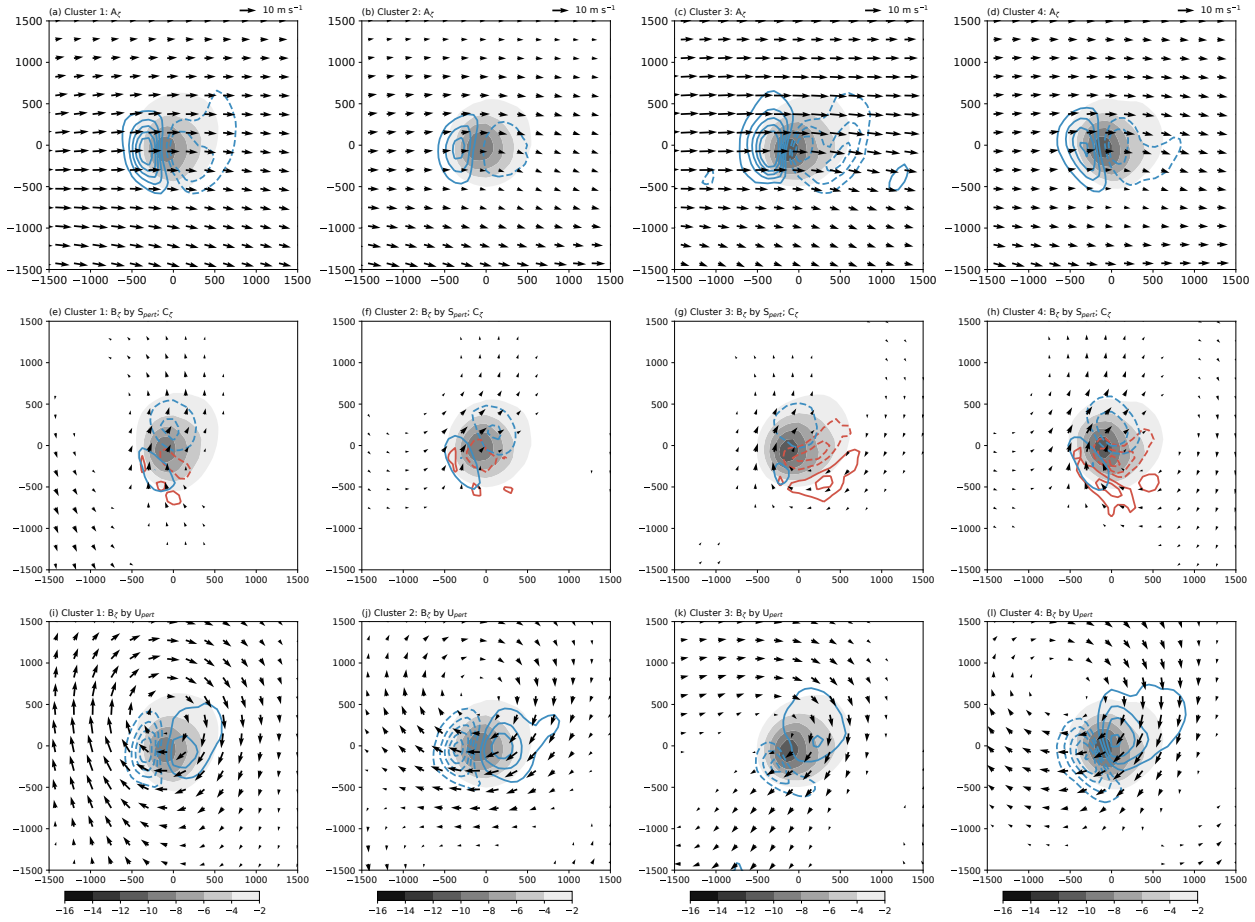


**Figure 9.** Composite fields of the 900–700 hPa vorticity tendency according to equation 6 at maximum intensity. (a–d) $A_\zeta$, (e–h) $B_\zeta$ by $S_{pert}$, and (i–l) $B_\zeta$ by $U_{pert}$ (blue contours every $5{\cdot}10^{-10}$ $s^{-2}$, negative values are dashed), (e–h) $C_\zeta$ term (red contours every $2{\cdot}10^{-10}$ $s^{-2}$, negative values are dashed), and relative vorticity (shading in $10^{-5}$ s$^{-1}$). Vectors denote (a–d) $(\bar{u}, \bar{v})$, (e–h) $(u', v')$ induced by $S_{pert}$, and (i–l) $(u', v')$ induced by $U_{pert}$. Wind vectors are only shown where wind speed greater than 2 m s$^{-1}$.

the divergence of the vorticity advective flux related to wind anomalies $(u', v')$ that are induced by these PV perturbation fields. As the wind anomalies associated with $M_{pert}$ are collocated with the cyclone centre in all clusters (middle row in Fig. 4), their contribution is negligible and not considered further. The divergence of the vorticity advective flux due to the time-mean basic state wind and the wind anomalies will be referred to as $A_\zeta$ and $B_\zeta$ respectively. The remaining terms on the right-hand side describe the effects of the non-advective-tilting flux. These terms are referred to as $C_\zeta$. In contrast to related studies (e.g., Coronel *et al.* 2015), we use the flux form of the vorticity tendency equation since splitting the divergence of the vorticity flux may cause non-cancelling errors leading to incorrect physical interpretations (Haynes and McIntyre 1987). In the following, the terms in equation 6 are calculated for the 900–700-hPa layer at maximum cyclone intensity.

At the time of maximum intensity, a characteristic common to the cyclones in each cluster is the eastward advection by the basic state (Figs. 9a–d); this advection is weakest for Cluster 2 and strongest for Cluster 3. Other features common to all clusters are the negative (cyclonic) vorticity tendencies south and east of the cyclone centre and in the region of the bent-back warm front due to $C_\zeta$ (red contours in Figs. 9e–h). Thus, $C_\zeta$ induces a cyclone displacement towards the south and east that is strongest for cyclones in Clusters 3 and 4. A southerly to southeasterly flow induced by $S_{pert}$ counteracts this displacement as indicated by positive (negative) vorticity tendencies through convergence (divergence) of the absolute vorticity advective flux (blue contours in Figs. 9e–h) to the south (north) of the low-level vorticity maximum. For Cluster 1, the lower-tropospheric circulation induced by $U_{pert}$ is displaced to the north of the cyclone centre (Fig. 9i). Hence, a strong easterly flow across the cyclone centre counteracts its eastward motion. For Cluster 2 cyclones, a strong easterly flow induced by the $U_{pert}$ anomaly that is located north of the cyclone centre strongly counteracts the eastward advection by the basic state (Fig. 9j). Compared

 

to all other clusters, the east–west dipole of advective fluxes by $U_{pert}$ is strongest for Cluster 2 cyclones. Combined with the weakest advective flux by the time-mean basic state, this coincides with the slowest eastward motion. In Cluster 3, the upstream upper-level trough and the downstream upper-level ridge induce a northeasterly flow across the cyclone centre (Fig. 9k). This flow counteracts the eastward displacement by the basic state and advects the cyclone poleward. The vorticity tendencies in Clusters 3 and 4 are structurally similar though the vorticity tendencies of $B_\zeta$ induced by $U_{pert}$ are considerably stronger (cf. Figs. 9k, l). The strong northeasterly flow across the cyclone counteracts its eastward displacement by the time-mean basic state and thus explains the reduced zonal displacement compared to Cluster 3 (cf. Figs. 5c, d). On the other hand, it is this northeasterly flow that also contributes to the largest poleward displacement of all clusters.

At 24 h, the magnitude of $B_\zeta$ and $C_\zeta$ are considerably weaker (not shown). It should be noted, however, that the dipole axis of the advective fluxes by $U_{pert}$ are much more zonally oriented in Clusters 2–4 than before. This is in agreement with the slower poleward displacement after maximum intensity (Fig. 5b–d) and with findings by Coronel *et al.* (2015). In an idealised setup they found that the dipole led to a more poleward displacement of the cyclone at early stages of the life cycle than at later stages. They attributed the rotation of the dipole axis to the cyclonic wind field of the cyclone itself.

In the following, we briefly expand on the idea that the effect of the upper-level PV anomalies on the advection of HCs can be viewed as a baroclinic analogue to the beta effect used to explain the poleward movement of tropical cyclones (Chan and Williams 1987). In brief, the differential advection of the Earth's vorticity by the tropical cyclone itself creates a cyclonic gyre to the west and an anticyclonic gyre to the east. These beta gyres weaken with height as the cyclonic circulation of the tropical cyclone itself weakens with height. Due to the development of an anticyclone in the upper-tropospheric outflow layer of the tropical cyclone, the beta gyres can flip, giving an analogy to a baroclinic beta gyre. The cyclonic (anticyclonic) gyres to the west (east) of the tropical cyclone induce an east–west asymmetry in the meridional wind field which advects the tropical cyclone poleward and westward. Chan and Williams (1987) showed that this poleward and westward displacement increases with an increase of the tropical cyclone intensity. In addition, the tropical cyclone displacement due to the beta effect decreases strongly with an increasing initial latitude of the cyclone (Wang and Li 1992). For HCs considered in this study, these two relationships are not found. Although cyclones in Clusters 3 and 4 are on average up to 0.5 CVU more intense than cyclones in Clusters 1 and 2 (not shown), the difference in low-level vorticity is only statistically significantly different between cyclones in Clusters 1 and 4 according to a Kruskal-Wallis post-hoc pairwise Dunn's test. Also, the poleward moving cyclones in Clusters 3 and 4 reach their peak intensity furthest poleward (not shown), actually implying a slower poleward displacement than for Clusters 1 and 2 according to the observed beta effect on tropical cyclones.

## 4. Concluding discussion

The work reported here is the first to analyse the dynamics of the intensity and motion of HCs in a composite PV framework. Using 573 cyclones that occurred in the Australian region during MJJAS 1979–2010 and PPVI, we quantify the contribution of individual PV anomalies to the intensity and motion of HCs around the time of maximum intensity. The analysis is performed on 4 clusters of cyclones that are identified from the structure of the 315-K PV anomaly. Physically, these clusters are interpreted as representing a north–south elongated trough (182 cyclones in Cluster 1), a PV cut-off (137 cyclones in Cluster 2), and cyclonically breaking troughs (111 and 143 cyclones in Clusters 3 and 4, respectively). Strikingly, clustering the 315-K PV anomaly yields the most distinct and significantly different cyclone tracks around maximum intensity compared to other PV-based cluster variables.

Cyclones in Cluster 1 reach their maximum intensity in a highly amplified flow with a pronounced upstream ridge and a north–south elongated trough. The circulation associated with this trough contributes more than 50% to the maximum cyclone intensity which is the strongest contribution of all clusters. Hence, we conclude that the intensity of cyclones in Cluster 1 is dominated by their corresponding upper-tropospheric cyclonic PV anomaly. Although the upper-tropospheric cyclonic PV anomaly

counteracts the eastward motion induced by the time-mean basic state, cyclones in Cluster 1 move rapidly eastward and slightly equatorward.

Cyclones in Cluster 2 are associated with an upper-tropospheric PV cut-off equatorward of a broad upper-tropospheric ridge. About one-third of the maximum cyclone intensity can be attributed to the cyclonic PV anomaly associated with the PV cut-off. The eastward motion of cyclones in Cluster 2 is considerably slower than in Cluster 1. The slower eastward motion is due to a comparatively weak westerly background flow and a strong easterly flow across the cyclone centre induced by the upper-level cyclonic PV anomaly.

Cyclones that form Cluster 3 are associated with a cyclonically breaking trough. The upstream trough and its cyclonic PV anomaly are displaced westward relative to the low-level cyclone centre. Hence, the upper-level PV anomalies account for less than one-third of the maximum cyclone intensity whereas the contribution from the interior layer and the surface layer reaches nearly 60%. Similar to cyclones in Cluster 1, Cluster 3 cyclones move rapidly eastward but slightly poleward. The poleward component is due to a northeasterly flow across the cyclone centre induced by the upstream trough and the downstream ridge.

Although cyclones in Cluster 4 are associated with a cyclonically breaking trough also, differences to Cluster 3 are noteworthy. With nearly two-thirds, the contribution from the interior layer and the surface layer to the cyclone intensity is even stronger. The strong contribution from the interior layer is reflected in the environment in which the cyclones develop. They reach their peak intensity in the moistest environment compared to the remaining clusters. Accordingly, they are associated with the strongest mean precipitation. Diabatic processes generate cyclonic PV in the low- to mid-troposphere, which is reflected by the most cyclonic PV anomaly in this layer relative to the remaining clusters. Of all clusters, cyclones in Cluster 4 exhibit the strongest poleward motion. This is due to the strongest northeasterly flow across the cyclone centre induced by the cyclonically breaking trough and the pronounced downstream upper-tropospheric ridge.

That the low-level flow induced by upper-levels explains the poleward movement of midlatitude cyclones is in line with recent idealised experiments (e.g., Oruba *et al.* 2013; Coronel *et al.* 2015; Tamarin and Kaspi 2016) and a case study by Riviére *et al.* (2012). To the authors' knowledge, the present work is the first to examine these findings in a synoptic climatology framework. In simulations with an initial upper-level cyclonic disturbance upstream of the low-level cyclone centre, Coronel *et al.* (2015) found that the poleward motion of a cyclone was faster than those without an upstream upper-level disturbance. This movement was mostly due to the nonlinear advection by the low-level flow induced by the upstream trough and the downstream ridge at upper-levels. Likewise, Tamarin and Kaspi (2016) showed in an idealised zonally symmetric moist general circulation model that it is the upper-level PV anomalies which advect the cyclone poleward. Hence, the advection of the cyclone by the upper-level PV anomalies can be viewed as a baroclinic analogue to the barotropic beta effect which has been used to explain the poleward movement of tropical cyclones (Chan and Williams 1987). In contrast to tropical cyclones, a dependence of the poleward motion on the intensity and latitude of the HCs is not found. Coronel *et al.* (2015) and Tamarin and Kaspi (2016) observed that the poleward motion of the cyclone was faster at early stages of the life cycle. This result is most consistent with the observed tracks for Cluster 4 cyclones. As in Coronel *et al.* (2015), we attribute the change in speed of the poleward movement to a rotation of the axis of the circulation dipole induced by the upstream trough and the downstream ridge.

The conclusions drawn from this study are valid only for HCs around Australia. It may be that the consistency between this study and previous idealised studies concerning the cyclone motion is specific to the baroclinic-channel-like flow conditions in the Southern Hemisphere. For example, it has been shown by Reeder *et al.* (1991) that baroclinic instability and frontogenesis described by a channel model agree remarkably well in detail with observations taken in the Australian region. Hence, an intriguing research opportunity may be to extend the analysis to the global scale and to elaborate regional differences concerning the dynamics and motion of HCs.

Finally, the clusters of HCs may differ in terms of their geographical distribution. For example, preliminary results suggest that cyclones in Cluster 4 occur considerably more frequently over the Tasman Sea than over the Great Australian

 

Bight. A detailed analysis of the geographical and seasonal distribution of the individual clusters, as well as of their relation to extreme winds and precipitation is left for future work.

*Acknowledgement*

We are thankful to Lance Bosart, Christian Grams, Heini Wernli and an anonymous reviewer for valuable comments and suggestions. The contribution of JFQ was partly funded by the Helmholtz-Association (grant VH-NG-1243). MJR gratefully acknowledges funding provided by the Australian Research Council Centre of Excellence for Climate Extremes (CE170100023). JLC was funded by the ARC Discovery Early Career Researcher Award grant DE140101305. We thank the Australian National Computational Infrastructure and ECMWF for providing access to the ERA-Interim reanalysis data.

## References

Ahmadi-Givi F, Graig GC, Plant RS. 2004. The dynamics of a midlatitude cyclone with very strong latent-heat release. *Q. J. R. Meteorol. Soc.* **130**(596 PART A): 295–323, doi:10.1256/qj.02.226.

Balasubramanian G, Yau MK. 1994. The effects of convection on a simulated marine cyclone. *J. Atmos. Sci.* **51**(16): 2397–2417, doi:10.1175/1520-0469(1994)051⟨2397:TEOCOA⟩2.0.CO;2.

Binder H, Boettcher M, Joos H, Wernli H, Binder H, Boettcher M, Joos H, Wernli H. 2016. The role of warm conveyor belts for the intensification of extratropical cyclones in Northern Hemisphere winter. *J. Atmos. Sci.* **73**(10): 3997–4020, doi:10.1175/JAS-D-15-0302.1.

Booth JF, Dunn-Sigouin E, Pfahl S. 2017. The relationship between extratropical cyclone steering and blocking along the North American East Coast. *Geophys. Res. Lett.* **44**(23): 11,976–11,984, doi:10.1002/2017GL075941.

Čampa J, Wernli H. 2012. A PV perspective on the vertical structure of mature midlatitude cyclones in the Northern Hemisphere. *J. Atmos. Sci.* **69**(2): 725–740, doi:10.1175/JAS-D-11-050.1.

Carlson TN. 1980. Airflow through midlatitude cyclones and the comma cloud pattern. *Mon. Weather Rev.* **108**(10): 1498–1509, doi:10.1175/1520-0493(1980)108⟨1498:ATMCAT⟩2.0.CO;2.

Catto JL. 2018. A new method to objectively classify extratropical cyclones for climate studies: testing in the southwest Pacific region. *J. Clim.* **31**: 4683–4704, doi:https://doi.org/10.1175/JCLI-D-17-0746.1.

Chan JCL, Williams RT. 1987. Analytical and numerical studies of the beta-effect in tropical cyclone motion. Part I: zero mean flow. *J. Atmos. Sci.* **44**(9): 1257–1265, doi:10.1175/1520-0469(1987)044⟨1257:AANSOT⟩2.0.CO;2.

Charney J. 1955. The use of the primitive equations of motion in numerical prediction. *Tellus* **7**(1): 22–26, doi:10.1111/j.2153-3490.1955.tb01138.x.

Coronel B, Ricard D, Rivière G, Arbogast P. 2015. Role of moist processes in the tracks of idealized midlatitude surface cyclones. *J. Atmos. Sci.* **72**(8): 2979–2996, doi:10.1175/JAS-D-14-0337.1.

Davis CA. 1992. A potential-vorticity diagnosis of the importance of initial structure and condensational heating in observed extratropical cyclogenesis. *Mon. Weather Rev.* **120**(11): 2409–2428, doi:10.1175/1520-0493(1992)120⟨2409:APVDOT⟩2.0.CO;2.

Davis CA, Emanuel KA. 1991. Potential vorticity diagnostics of cyclogenesis. *Mon. Weather Rev.* **119**(8): 1929–1953, doi:10.1175/1520-0493(1991)119⟨1929:PVDOC⟩2.0.CO;2.

Davis CA, Grell ED, Shapiro MA. 1996. The balanced dynamical nature of a rapidly intensifying oceanic cyclone. *Mon. Weather Rev.* **124**: 3–26, doi:10.1175/1520-0493(1996)124⟨0003:TBDNOA⟩2.0.CO;2.

Dee DP, Uppala SM, Simmons AJ, Berrisford P, Poli P, Kobayashi S, Andrae U, Balmaseda MA, Balsamo G, Bauer P, Bechtold P, Beljaars ACM, van de Berg L, Bidlot J, Bormann N, Delsol C, Dragani R, Fuentes M, Geer AJ, Haimberger L, Healy SB, Hersbach H, Hólm EV, Isaksen L, Kållberg P, Köhler M, Matricardi M, Mcnally AP, Monge-Sanz BM, Morcrette JJ, Park BK, Peubey C, de Rosnay P, Tavolato C, Thépaut JN, Vitart F. 2011. The ERA-Interim reanalysis: configuration and performance of the data assimilation system. *Q. J. R. Meteorol. Soc.* **137**(656): 553–597, doi:10.1002/qj.828.

Evans C, Wood KM, Aberson SD, Archambault HM, Milrad SM, Bosart LF, Corbosiero KL, Davis CA, Dias Pinto JR, Doyle J, Fogarty C, Galarneau TJ, Grams CM, Griffin KS, Gyakum J, Hart RE, Kitabatake N, Lentink HS, McTaggart-Cowan R, Perrie W, Quinting JFD, Reynolds CA, Riemer M, Ritchie EA, Sun Y, Zhang F. 2017. The extratropical transition of tropical cyclones. Part I: cyclone evolution and direct impacts. *Mon. Weather Rev.* : MWR–D–17–0027.1doi:10.1175/MWR-D-17-0027.1.

Evans JL, Guishard MP. 2009. Atlantic subtropical storms. Part I: diagnostic criteria and composite analysis. *Mon. Weather Rev.* **137**(7): 2065–2080, doi:10.1175/2009MWR2468.1.

Evans JL, Hart RE. 2003. Objective indicators of the life cycle evolution of extratropical transition for Atlantic tropical cyclones. *Mon. Weather Rev.* **131**(5): 909–925, doi:10.1175/1520-0493(2003)131⟨0909:OIOTLC⟩2.0.CO;2.

Gilet JB, Plu M, Rivière G. 2009. Nonlinear baroclinic dynamics of surface cyclones crossing a zonal jet. *J. Atmos. Sci.* **66**(10): 3021–3041, doi:10.1175/2009JAS3086.1.

Grams CM, Wernli H, Böttcher M, Čampa J, Corsmeier U, Jones SC, Keller JH, Lenz CJ, Wiegand L. 2011. The key role of diabatic processes in modifying the upper-tropospheric wave guide: a North Atlantic case-study. *Q. J. R. Meteorol. Soc.* **137**(661): 2174–2193, doi:10.1002/qj.891.

Griffiths M, Reeder MJ, Low DJ, Vincent RA. 1998. Observations of a cut-off low over southern Australia. *Q. J. R. Meteorol. Soc.* **124**(548): 1109–1132,

 

doi:10.1002/qj.49712454805.

Harrold TW. 1973. Mechanisms influencing the distribution of precipitation within baroclinic disturbances. *Q. J. R. Meteorol. Soc.* **99**(420): 232–251, doi:10.1002/qj.49709942003.

Hart RE. 2003. A cyclone phase space derived from thermal wind and thermal asymmetry. *Mon. Weather Rev.* **131**(4): 585–616, doi:10.1175/1520-0493(2003)131⟨0585:ACPSDF⟩2.0.CO;2.

Hartigan JA, Wong MA. 1979. Algorithm AS 136: a k-means clustering algorithm. *Appl. Stat.* **28**(1): 100, doi:10.2307/2346830.

Haynes PH, McIntyre ME. 1987. On the evolution of vorticity and potential vorticity in the presence of diabatic heating and frictional or other forces. *J. Atmos. Sci.* **44**(5): 828–841, doi:10.1175/1520-0469(1987)044⟨0828:OTEOVA⟩2.0.CO;2.

Hodges KI. 1994. A general-method for tracking analysis and its application to meteorological data. *Mon. Weather Rev.* **122**(11): 2573–2586, doi:10.1175/1520-0493(1994)122⟨2573:AGMFTA⟩2.0.CO;2.

Hodges KI. 1995. Feature tracking on the unit sphere. *Mon. Weather Rev.* **123**(12): 3458–3465, doi:10.1175/1520-0493(1995)123⟨3458:FTOTUS⟩2.0.CO;2.

Hodges KI. 1999. Adaptive constraints for feature tracking. *Mon. Weather Rev.* **127**(6): 1362–1373, doi:10.1175/1520-0493(1999)127⟨1362:ACFFT⟩2.0.CO;2.

Hoskins BJ. 1990. Theory of extratropical cyclones. In: *Extratropical Cyclones Erik Palmen Meml. Vol.*, Newton C, Holopainen EO (eds), Am. Meteorol. Soc.: Boston, Mass., pp. 63–80.

Hoskins BJ, McIntyre ME, Robertson AW. 1985. On the use and significance of isentropic potential vorticity maps. *Q. J. R. Meteorol. Soc.* **111**(6): 877–946, doi:10.1002/qj.49711147002.

Jones SC, Harr PA, Abraham J, Bosart LF, Bowyer PJ, Evans JL, Hanley DE, Hanstrum BN, Hart RE, Lalaurette F, Sinclair MR, Smith RK, Thorncroft C. 2003. The extratropical transition of tropical cyclones: forecast challenges, current understanding, and future directions. *Weather Forecast.* **18**(6): 1052–1092, doi:10.1175/1520-0434(2003)018⟨1052:TETOTC⟩2.0.CO;2.

Kruskal WH, Wallis A. 1952. Use of ranks in one-criterion variance analysis. *J. Am. Stat. Assoc.* **47**(260): 583–621.

Kuo YH, Shapiro MA, Donall EG. 1991. The interaction between baroclinic and diabatic processes in a numerical simulation of a rapidly intensifying extratropical marine cyclone. *Mon. Weather Rev.* **119**(2): 368–384, doi:10.1175/1520-0493(1991)119⟨0368:TIBBAD⟩2.0.CO;2.

Lee YY, Grotjahn R. 2016. California Central Valley summer heat waves form two ways. *J. Clim.* **29**(3): 1201–1217, doi:10.1175/JCLI-D-15-0270.1.

Martin J, Otkin J. 2004. The rapid growth and decay of an extratropical cyclone over the central Pacific Ocean. *Weather Forecast.* **19**: 358–376.

Martin JE, Marsili N. 2002. Surface cyclolysis in the North Pacific ocean. Part II: piecewise potential vorticity diagnosis of a rapid cyclolysis event. *Mon. Weather Rev.* **130**(5): 1264–1281, doi:10.1175/1520-0493(2002)130⟨1264:SCITNP⟩2.0.CO;2.

Massacand AC, Wernli H, Davies HC. 2001. Influence of upstream diabatic heating upon an Alpine event of heavy precipitation. *Mon. Weather Rev.* **129**(11): 2822–2828, doi:10.1175/1520-0493(2001)129⟨2822:IOUDHU⟩2.0.CO;2.

Mills GA. 2001. Mesoscale cyclogenesis in reversed shear: the 1998 Sydney to Hobart yacht race storm. *Aust. Meteorol. Mag. Canberra, Aust.* **50**(1): 29–52.

Mills GA, Webb R, Davidson NE, Kepert J, Seed A, Abbs D. 2010. The Pasha Bulker east coast low of 8 June 2007. Technical Report June, CAWCR.

Mills GA, Wu BJ. 1995. The 'Cudlee Creek' flash-flood: an example of synoptic-scale forcing of a mesoscale event. *Aust. Meteorol. Mag. Canberra, Aust.* **44**(3): 201–218.

Oruba L, Lapeyre G, Rivière G. 2013. On the poleward motion of midlatitude cyclones in a baroclinic meandering jet. *J. Atmos. Sci.* **70**(8): 2629–2649, doi:10.1175/JAS-D-12-0341.1.

Pomroy HR, Thorpe AJ. 2000. The evolution and dynamical role of reduced upper-tropospheric potential vorticity in intensive observing period one of FASTEX. *Mon. Weather Rev.* **128**: 1817–1834, doi:10.1175/1520-0493(2000)128⟨1817:TEADRO⟩2.0.CO;2.

Quinting JF, Catto JL, Reeder MJ. 2018. Synoptic climatology of hybrid cyclones in the Australian region. *Q. J. R. Meteorol. Soc.* **submitted**.

Reed RJ, Stoelinga MT, Kuo YH. 1992. A model-aided study of the origin and evolution of the anomalously high potential vorticity in the inner region of a rapidly deepening marine cyclone. *Mon. Weather Rev.* **120**(6): 893–913, doi:10.1175/1520-0493(1992)120⟨0893:AMASOT⟩2.0.CO;2.

Reeder MJ, Keyser D, Schmidt BD. 1991. Threedimensional baroclinic instability and summertime frontogenesis in the Australian region. *Q. J. R. Meteorol. Soc.* **117**(497): 1–28, doi:10.1002/qj.49711749702.

Riviére G, Arbogast P, Lapeyre G, Maynard K. 2012. A potential vorticity perspective on the motion of a mid-latitude winter storm. *Geophys. Res. Lett.* **39**(12): 2–7, doi:10.1029/2012GL052440.

Rossa MA, Wernli H, Davies CH. 2000. Growth and decay of an extra-tropical cyclone's PV-tower. *Meteorol. Atmos. Phys.* **73**(3): 139–156, doi:10.1007/s007030050070.

Shapiro MA, Keyser D. 1990. Fronts, jet streams and the tropopause. In: *Extratropical Cyclones Erik Palmen Meml. Vol.*, Newton CW, Holopainen EO (eds), Am. Meteorol. Soc.: Boston, Mass., pp. 167–191.

Simpson RH. 1952. Evolution of the Kona storm, a subtropical cyclone. *J. Meteorol.* **9**(1): 24–35, doi:10.1175/1520-0469(1952)009⟨0024:EOTKSA⟩2.0.CO;2.

Spiegler DB. 1972. Cyclone categories and definitions: some proposed revisions. *Bull. Am. Meteorol. Soc.* **53**(12): 1174–1178.

Stefanon M, D'Andrea F, Drobinski P. 2012. Heatwave classification over Europe and the Mediterranean region. *Environ. Res. Lett.* **7**(1): 014 023, doi:10.1088/1748-9326/7/1/014023.

Stoelinga MT. 1996. A potential vorticity-based study of the role of diabatic heating and friction in a numerically simulated baroclinic cyclone. *Mon.*

 

*Weather Rev.* **124**(5): 849–874, doi:10.1175/1520-0493(1996)124⟨0849:APVBSO⟩2.0.CO;2.

Tamarin T, Kaspi Y. 2016. The poleward motion of extratropical cyclones from a potential vorticity tendency analysis. *J. Atmos. Sci.* **73**: 1687–1707, doi:10.1175/JAS-D-15-0168.1.

Tamarin-Brodsky T, Kaspi Y. 2017. Enhanced poleward propagation of storms under climate change. *Nat. Geosci.* **10**(12): 908–913, doi:10.1038/s41561-017-0001-8.

Teubler F, Riemer M. 2015. Dynamics of Rossby wave packets in a quantitative potential vorticity-potential temperature framework. *J. Atmos. Sci.* **73**(3): 1063–1081, doi:10.1175/JAS-D-15-0162.1.

Wang B, Li X. 1992. The beta drift of three-dimensional vortices: a numerical study. *Mon. Weather Rev.* **120**(4): 579–593, doi:10.1175/1520-0493(1992)120⟨0579:TBDOTD⟩2.0.CO;2.

Wernli H, Davies HC. 1997. A Lagrangian-based analysis of extratropical cyclones: The method and some applications. *Q. J. R. Meteorol. Soc.* **123**(538): 467–489, doi:10.1256/smsqj.53810.

 